THE EUROPEAN
PHYSICAL JOURNAL C

Quantum interference effects in Higgs boson pair-production beyond the standard model

Biswaranjan Das[1,2,a], **Stefano Moretti**[3,b], **Shoaib Munir**[1,c] , **Poulose Poulose**[4,5,d]

[1] East African Institute for Fundamental Research (ICTP-EAIFR), University of Rwanda, Kigali, Rwanda
[2] Center for Fundamental Physics, Zewail City of Science and Technology, 6 October City, Giza, Egypt
[3] School of Physics and Astronomy, University of Southampton, Highfield, Southampton SO17 1BJ, UK
[4] Department of Physics, IIT Guwahati, Guwahati, Assam 781039, India
[5] Department of Physics, Concordia University, Montreal, QC H4B 1R6, Canada

Abstract New physics frameworks like the next-to-minimal supersymmetric standard Model and the Next-to-2-Higgs-doublet Model contain three neutral CP-even Higgs bosons. It is possible for the heavier two of these states to have masses identical to each other, which can result in a sizeable quantum interference between their propagators in processes they mediate. For both these models, we study the impact of such interference on the pair-production of the lightest of the three scalars, which we identify with the observed 125 GeV Higgs boson, in the gluon-fusion channel at the large hadron collider (LHC). We find that the inclusion of these effects can substantially alter the cross section, compared to its value when they are ignored, for this process. Our results illustrate the importance of taking possible quantum interference effects into account not only when investigating the phenomenology of extended Higgs sectors at the future Run(s) of the LHC, but also when imposing its current exclusion bounds on the parameter spaces of these models.

1 Introduction

Pair-production of the Higgs boson state, h_{obs}, discovered in 2012 [1,2] is a key process for measuring the Higgs self-coupling at the Run 3 of the large hadron collider (LHC), as well as at its now approved high-luminosity upgrade (HL-LHC). This process represents a direct probe of the mechanism of electroweak symmetry breaking (EWSB), since the Higgs self-coupling enters the Higgs potential directly.

Accessing it experimentally will thus be of extreme importance in order to understand whether mass generation in nature occurs within the Standard Model (SM) or in some scenario incorporating new physics.

In a beyond-the-SM (BSM) framework containing an extended Higgs sector, the phenomenology of the pair-production process of the h_{obs} candidate, i.e., the Higgs boson with mass lying near 125 GeV, can deviate significantly from that in the SM due to two main reasons. First, the h_{obs} self-coupling gets modified from its predicted value in the SM owing to the mixing between various interaction eigenstates. Secondly, the additional Higgs states also enter the resonant channel, so that the other Higgs trilinear couplings appearing in the Lagrangian of the model also come into play. While there exists plenty of literature on h_{obs} pair-production in BSM scenarios at the various energy and luminosity stages of the LHC, most often this is limited to frameworks wherein only one CP-even companion to the SM-like Higgs state exists, like the 2-Higgs Doublet Model (2HDM) [3] or the Minimal Supersymmetric Standard Model (MSSM) [4,5].

In the MSSM, the requirement for the lighter of its two scalar states, H_1, to be a good h_{obs} candidate pushes the heavier scalar, H_2, as well as the solo pseudoscalar, A, up into the so-called decoupling regime [6], where they have identical masses.[1] If the MSSM Higgs sector is CP-violating, all the interaction eigenstates can mix together to yield three CP-indefinite physical states, with the two nearly mass-degenerate heavy states now labelled H_2 and H_3. When the mass-splitting between these two is comparable to the sum of their widths, a description of the intervening propagators which takes into account the imaginary parts of the one-loop self-energies, alongside the customary real

[a] e-mail: bdas@zewailcity.edu.eg

[b] e-mail: s.moretti@soton.ac.uk

[c] e-mail: smunir@eaifr.org (corresponding author)

[d] e-mail: poulose@iitg.ac.in

---

[1] Alternatively, the H_1 can have SM-like properties in the 'alignment without decoupling' scenario [7–9] also.

parts, becomes necessary [10,11]. This is because the imaginary off-diagonal entries of the Higgs propagator matrix can induce quantum interference between these states, so that the one produced in, for example, gluon-fusion can potentially oscillates into the other one before decaying into a given SM final state. This can significantly alter not only the total production cross section but also the shape of the differential cross section distribution for that final state [12,13].

In the 2-Higgs-doublet model (2HDM), obtained by simply adding an additional Higgs doublet to the SM, which results again in two scalar and one pseudoscalar Higgs states, a mass-degeneracy between H_2 and A is not a precondition for the H_1 to have properties identical to the h_{obs}. It is nonetheless a possibility not ruled out by any experimental results, and the aforementioned interference effects can become significant in this model also if it has a CP-violating Higgs sector with $m_{H_2} \approx m_{H_3}$. In a BSM scenario containing three or more CP-even Higgs bosons, the quantum interference effects can appear in processes involving Higgs propagators without the need to invoke CP-violation. A minimal realisation of such a scenario would be the extension of the two models mentioned above by a singlet Higgs field, resulting in an extra scalar state in their Higgs sectors.

In the context of supersymmetry, adding a complex singlet Higgs field to the MSSM can address some of its theoretical and phenomenological shortcomings, resulting in the so-called Next-to-MSSM (NMSSM) [14–17]. In this model, some particular configurations of the free parameters can yield a SM-like H_1 along with H_2 and H_3 that are nearly mass-degenerate. We have previously investigated the aforementioned interference effects in the NMSSM, in the scenario where H_1 and H_2 are mass-degenerate [18], as well as in the alternative scenario with $m_{H_2} \approx m_{H_3}$ [19]. The first study pertained to the production process for the $\gamma\gamma$ final state and the second to that of $\tau^+\tau^-$ at the LHC. Both these studies found the results from the calculation embedding the full Higgs propagator matrix to be notably different from the ones using the standard approximation where only one term containing a Breit–Wigner (BW) propagator corresponding to each of the Higgs bosons appears in the amplitude expression. It was also shown in those papers that the expected mass resolutions of the respective final states at the LHC may, however, not allow it to disentangle the two Higgs states from each other.

In this article, we investigate the implications of the quantum interference on the gluon-initiated pair-production of the SM-like H_1 state of the NMSSM at the LHC with $\sqrt{s} = 14$ TeV, and also of its non-supersymmetric counterpart, the next-to-2HDM (N2HDM). The latter model is obtained by introducing a real singlet Higgs field into the 2HDM, and while it is phenomenologically similar to the NMSSM, a crucial advantage the N2HDM has is that the physical Higgs boson masses can themselves be the input

parameters. This grants us the freedom of setting the H_2 and H_3 masses exactly equal and assessing the impact of this maximal mass-degeneracy on the said process. This model additionally allows us to analyse how the various Higgs couplings govern the relative sizes of the interference effects, so that the general inferences can be extended to other multi-Higgs BSM scenarios.

The article is organised as follows. In the next section we briefly revisit the Higgs pair-production process at the LHC. In Sect. 3 we discuss some details of the NMSSM and the N2HDM, as well as of our numerical computational tool. In Sect. 4 we present our analysis and discuss its results. In Sect. 5 we conclude our findings.

2 Higgs pair-production at the LHC

The cross section for the (inclusive) process $pp \to H_i H_j$, where $i, j = 1, ..., N$ for a model with N CP-even Higgs bosons but without any additional particle content beyond the SM, can be written at the leading order (LO) as

$$\sigma_{\text{LO}}(pp \to H_i H_j)$$
$$= \int_0^1 d\tau \int_\tau^1 \frac{dx_1}{x_1} \frac{g(x_1)g(\tau/x_1)}{1024\pi \hat{s}^3} \mathcal{A}^2_{gg \to H_i H_j}, \quad (1)$$

where $g(x_1)$ and $g(x_2)$ are the parton distribution functions (PDFs) of the two incoming gluons having squared centre-of-mass (CM) energy $\hat{s} = x_1 x_2 s$, given in terms of the total CM energy, s, of the pp system, and by defining $\tau \equiv \frac{\hat{s}}{s} = x_1 x_2$. The amplitude-squared in Eq. (1) can be written, following the notation of Ref. [20], as

$$\mathcal{A}^2_{gg \to H_i H_j} = \left| C_\triangle F_\triangle + C_\square F_\square \right|^2 + \left| C_\square G_\square \right|^2, \quad (2)$$

where $\triangle$ denotes the contribution from the Higgs-mediated triangle loop diagram, Fig. 1 (left), and $\square$ refers to the quark-box diagram, Fig. 1 (right).

The coefficient corresponding to the box contributions in Eq. (2) is written in terms of the Yukawa couplings as

$$C_\square = \sum_q g_{H_i \bar{q} q} g_{H_j \bar{q} q}. \quad (3)$$

The form factor $F_\square$ corresponds to the case when the gluons have a combined total spin of $S_z = 0$ along the proton beam, while $G_\square$ refers to the case with $S_z = 2$. The full expressions for $F_\square$ and $G_\square$ within the SM can be found in the appendix of Ref. [20].
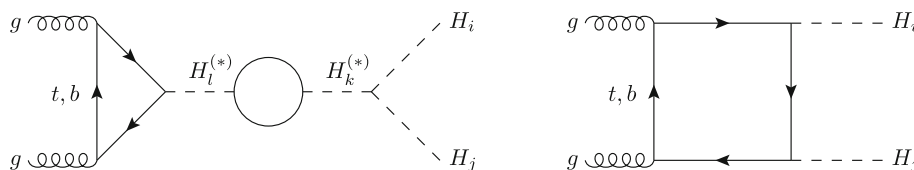
Fig. 1 The Feynman diagrams contributing to Higgs boson pair-production in a model with an extended Higgs sector, but no additional particle content besides the SM

The Higgs-mediated triangle loop diagram contributes only to the $S_z = 0$ case. The corresponding form factor, for state H_l attached to the triangle, is written as

$$F_\triangle^l = \frac{\alpha_s \hat{s}}{4\pi v} \left\{ S_l^g + i\lambda P_l^g \right\},\tag{4}$$

where the scalar and pseudoscalar components, S_l^g and P_l^g, respectively, can be found in, e.g., Refs. [21,22]. In case of a single Higgs boson, as in the SM, the triangle coefficient in Eq. (2) is given as

$$C_\triangle = \frac{M_Z^2}{\hat{s} - M_h^2} \lambda_{hhh},\tag{5}$$

where λ_{hhh} is the Higgs trilinear self-coupling. In multi-Higgs models like the ones we intend to explore here, the above coefficient is generalised to

$$C_\triangle^l \equiv \sum_{k=1}^{N} \mathcal{D}_{kl}(\hat{s}) \lambda_{H_i H_j H_k} .\tag{6}$$

Here, $\lambda_{H_i H_j H_k}$ are the Higgs trilinear couplings and $\mathcal{D}_{kl}(\hat{s})$, with $k, l = 1, ..., N$, are the entries of the Higgs propagator matrix. This modified $C_\triangle^l$ allows the possibility of interference between two different Higgs intermediate states, induced by higher order quantum effects, as illustrated by Fig. 1 (left).

The main focus of this study is to investigate the above-mentioned quantum effects in the specific scenario with $N = 3$, which permits the resonant pair-production of the lightest Higgs state via the two, mutually interfering, heavier states. In this scenario, the (symmetric) propagator matrix is written as

where the $\mathfrak{Im}\hat{\Pi}_{kl}(\hat{s})$ are the absorptive parts of the Higgs self-energies, and m_{H_k} is the renormalised mass of the k-th Higgs boson. The explicit expressions for $\mathfrak{Im}\hat{\Pi}_{kl}(\hat{s})$ can be found in the Appendix of Ref. [18]. In general, however, the off-diagonal absorptive terms in the propagator are assumed to be negligible, in which case the $\mathcal{D}(\hat{s})$ becomes a diagonal matrix and $C_\triangle$ can, to a good approximation, be reduced to a sum over three terms containing BW propagators corresponding to each H_l, as in Eq. (5).

3 Models and computational tools

Two new physics models that are consistent with the $N = 3$ scenario are the NMSSM and N2HDM. In both these models, we identified the lightest of the three scalars, H_1, with h_{obs}, and analysed the impact of the interference between the heavier H_2 and H_3 on its pair-production at the $\sqrt{s} = 14$ TeV LHC. It has previously been emphasised in literature [11,18,23,24] that these effects are more pronounced for large (combined) total widths of the intermediate Higgs states compared to the mass splitting between these. Using this as a guideline, we numerically scanned the parameter spaces of the two models to find their potentially relevant configurations. Below we discuss some details of the two models as well as of our calculation of the $H_1 H_1$ production cross section.

3.1 NMSSM

As a follow-up of our previous analyses, the first model that we investigate is the Z_3-symmetric NMSSM. The Higgs potential in this model is written in terms of the two $SU(2)_L$ doublets H_u and H_d, with $Y = \pm 1$, and the singlet S as

$$\mathcal{D}(\hat{s}) = \hat{s} \begin{pmatrix} \hat{s} - m_{H_1}^2 + i\mathfrak{Im}\hat{\Pi}_{11}(\hat{s}) & i\mathfrak{Im}\hat{\Pi}_{12}(\hat{s}) & i\mathfrak{Im}\hat{\Pi}_{13}(\hat{s}) \\ i\mathfrak{Im}\hat{\Pi}_{21}(\hat{s}) & \hat{s} - m_{H_2}^2 + i\mathfrak{Im}\hat{\Pi}_{22}(\hat{s}) & i\mathfrak{Im}\hat{\Pi}_{23}(\hat{s}) \\ i\mathfrak{Im}\hat{\Pi}_{31}(\hat{s}) & i\mathfrak{Im}\hat{\Pi}_{32}(\hat{s}) & \hat{s} - m_{H_3}^2 + i\mathfrak{Im}\hat{\Pi}_{33}(\hat{s}) \end{pmatrix}^{-1} ,\tag{7}$$

$$\begin{aligned}
V_{\text{NMSSM}} = &\left|\lambda\left(H_u^+ H_d^- - H_u^0 H_d^0\right) + \kappa S^2\right|^2 + m_S^2|S|^2 \\
&+ \left(m_{H_u}^2 + |\lambda S|^2\right)\left(|H_u^0|^2 + |H_u^+|^2\right) \\
&+ \left(m_{H_d^0}^2 + |\lambda S|^2\right)\left(|H_d^0|^2 + |H_d^-|^2\right) \\
&+ \frac{g_1^2 + g_2^2}{8}\left(|H_u^0|^2 + |H_u^+|^2 - |H_d^0|^2 - |H_d^-|^2\right)^2 \\
&+ \frac{g_2^2}{2}|H_u^+ H_d^{0*} + H_u^0 H_d^{-*}|^2 \\
&+ \left[\lambda A_\lambda\left(H_u^+ H_d^- - H_u^0 H_d^0\right)S + \frac{1}{3}\kappa A_\kappa S^3 + \text{h.c.}\right]. \quad (8)
\end{aligned}$$

Here λ and κ are dimensionless Higgs trilinear couplings and A_λ and A_κ are their respective soft SUSY-breaking counterparts, m_{H_d}, m_{H_u} and m_S are the soft Higgs masses, while g_1 and g_2 are the $U(1)_Y$ and $SU(2)_L$ gauge coupling constants, respectively.

The neutral components of the fields H_d, H_u and S are developed around their respective Vacuum Expectation Values (VEVs) v_d, v_u and v_S, when EW symmetry is broken, as

$$H_d^0 = \begin{pmatrix} v_d + H_{dR} + i H_{dI} \\ H_d^- \end{pmatrix},$$

$$H_u^0 = \begin{pmatrix} H_u^+ \\ v_u + H_{uR} + i H_{uI} \end{pmatrix}, \quad S = v_S + S_R + i S_I. \quad (9)$$

By taking the second derivative of V_{NMSSM}, one then obtains the tree-level 3×3 neutral CP-even Higgs mass-squared matrix, M_H^2, in the $(H_{dR}, H_{uR}, S_R)^T$ basis. The orthogonal matrix $\mathcal{R}$ rotates these interaction eigenstates into the physical states as

$$(H_1, H_2, H_3)^T = \mathcal{R}(H_{dR}, H_{uR}, S_R)^T . \quad (10)$$

The matrix M_H^2 thus gets diagonalised as

$$\mathcal{R} M_H^2 \mathcal{R}^T = \text{diag}\left(m_{H_1}^2, m_{H_2}^2, m_{H_3}^2\right), \quad (11)$$

with Higgs boson masses in the ascending order, i.e., $m_{H_1} < m_{H_2} < m_{H_3}$.

Our current analysis pertains to the 'phenomenological' NMSSM, wherein all the free parameters, including the above Higgs sector ones, are input at the EW scale. Since variations in non-Higgs sector parameters are expected to have little impact on our particular phenomenological scenario, we fixed the soft squark masses as $M_{Q_{1,2,3}} = M_{U_{1,2,3}} = M_{D_{1,2,3}} = 3\,\text{TeV}$, the slepton masses as $M_{L_{1,2,3}} = M_{E_{1,2,3}} = 2\,\text{TeV}$, the soft gaugino masses as $2M_1 = M_2 = \frac{1}{3}M_3 = 1\,\text{TeV}$. This resulted in $\tan\beta$ ($\equiv \frac{v_u}{v_d}$), μ_{eff} ($\equiv \lambda v_s$), λ, κ, m_P, m_A, and the unified trilinear coupling of the charged sfermions, $A_0 \equiv A_{\tilde{u},\tilde{c},\tilde{t}} = A_{\tilde{d},\tilde{s},\tilde{b}} = A_{\tilde{e},\tilde{\mu},\tilde{\tau}}$, as the complete set of inputs. The parameters m_P and m_A are the bare masses of the two pseudoscalars, which are a trade-off for A_λ and A_κ using the minimisation conditions of the Higgs potential.

Table 1 Ranges of the NMSSM input parameters scanned for obtaining H_2 and H_3 with large mass-degeneracy. The third column shows the parameter space yielding $m_{H_{2,3}} \leq 500\,\text{GeV}$

Parameter	Scanned range	Range giving $m_{H_{2,3}} \leq 500\,\text{GeV}$
A_0 (GeV)	−5000 to 0	−5000 to −3500
μ_{eff} (GeV)	100 to 1000	100 to 250
$\tan\beta$	1 to 40	5 to 10
λ	0.001 to 0.7	0.001 to 0.3
κ	0.001 to 0.7	0.001 to 0.5
m_P (GeV)	100 to 1000	100 to 500
m_A (GeV)	100 to 1000	400 to 500

We used the public code NMSSMTools-v5.5.2 [25–27] for numerically generating the Higgs boson mass spectra and branching ratios (BRs) corresponding to each set of values of the seven model input parameters, randomly selected from the ranges shown in the second column of Table 1. Each parameter space point was required to satisfy all the theoretical and experimental constraints defined in NMSSMTools, which include limits from the Higgs searches at the Large Electron–Positron (LEP) collider, the TeVatron and the LHC, from the direct and indirect searches for neutralino Dark Matter (DM) and estimates of its relic abundance and from B-physics measurements. In our scenario, since the H_1 plays the role of the h_{obs}, NMSSMTools intrinsically imposes 2σ bounds on its couplings from the most relevant recent LHC results, while also requiring m_{H_1} to lie within the $122 - 128\,\text{GeV}$ range, allowing a $\pm 3\,\text{GeV}$ theoretical uncertainty on the measured mass of $\sim 125\,\text{GeV}$. Output points satisfying all these constraints were further run through HiggsBounds-v5.7.0 [28–32] to test the Higgs sector observables of the model against the latest exclusion bounds from the LHC that might not (yet) have been included in NMSSTools itself.

In Fig. 2 we show the resulting successful points with $m_{H_{2,3}} \leq 500\,\text{GeV}$, which are obtained for the input parameter ranges given in the third column of Table 1. One notices that the limits from the direct searches at the LHC rule out a mass below $\sim 405\,\text{GeV}$ for the (predominantly doublet-like) H_3, over the entire parameter space explored. Our initial scan with wide input ranges of the parameters yielded only one point (out of nearly two thousand violet points in the figure) with $\Delta m_H \equiv m_{H_3} - m_{H_2}$ less than 5 GeV, lying just above the LHC exclusion bound for m_{H_3}. In order to find solutions with larger H_2-H_3 mass-degeneracy, we therefore performed another scan of the narrowed-down parameter space region around the said point. Indeed, several points with $\Delta m_H < 1\,\text{GeV}$ were obtained with this secondary scan, which are plotted in blue colour in the figure. The coordinates of the point with the smallest Δm_H are
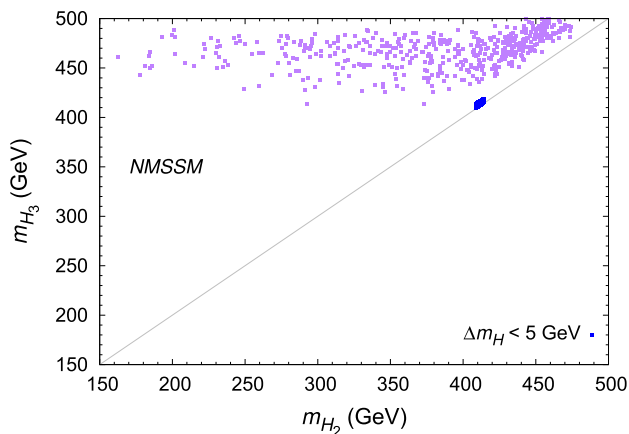
Fig. 2 The masses of H_2 and H_3 for the points obtained in the scans of the extended parameter space of the NMSSM (violet) and of its narrow region yielding $\Delta m_H < 5$ GeV (blue)

$$\tan\beta = 6, \quad A_0 = -5000\,\text{GeV}, \quad \lambda = 0.005, \quad \kappa = 0.0071,$$
$$\mu_{\text{eff}} = 148.24\,\text{GeV}, \quad m_P = 147.59\,\text{GeV},$$
$$m_A = 431.25\,\text{GeV}, \tag{12}$$

which result in the following Higgs mass spectrum:

$$m_{H_1} = 122.23\,\text{GeV}, \quad m_{H_2} = 409.33\,\text{GeV},$$
$$m_{H_3} = 410.13\,\text{GeV},$$
$$m_{A_1} = 147.59\,\text{GeV}, \quad m_{A_2} = 408.23\,\text{GeV},$$
$$m_{H^\pm} = 416.13\,\text{GeV}. \tag{13}$$

The total widths of the three scalars yielded by the above parameter space point are $\Gamma_{H_1} = 4.76$ MeV, $\Gamma_{H_2} = 535.4$ MeV and $\Gamma_{H_3} = 24.78$ MeV. H_2 in this point is doublet-like, while H_3 is singlet-like. For this reason, the latter has much weaker couplings to the SM, and hence much smaller partial decay widths, than the former. We also point out that for many points obtained in the initial wider scan, m_{H_1} easily reaches up to 125 GeV. Its lying close to the enforced lower limit of 122 GeV for the point in Eq. (13) is simply a consequence of the very narrow parameter space scanned to obtain maximally degenerate m_{H_2} and m_{H_3}, especially with the soft squark and gaugino masses fixed. For this point, the A_0 parameter, larger magnitudes of which were generally preferred by the points in order to push m_{H_1} above 122 GeV, sits right at the upper end of its scanned range.

3.2 N2HDM

Since the scans for the NMSSM did not generate any points with a H_3 lighter than ~ 405 GeV, we extended our analysis to the N2HDM also. In this model the physical masses of the three scalar Higgs bosons, m_{H_i}, are input parameters, as opposed to the NMSSM, wherein they are derived quantities, which allows greater freedom in the selection of the other free

parameters relevant to the process under investigation. The N2HDM is obtained by adding a real singlet scalar field, S, to the (CP-conserving) 2HDM, and its Higgs potential reads

$$
\begin{aligned}
V_{\text{N2HDM}} = {} & m_{H_u}^2 |H_u|^2 + m_{H_d}^2 |H_d|^2 - m_{12}^2 \left(H_u^\dagger H_d + \text{h.c.} \right) \\
& + \frac{\lambda_1}{2} \left(H_u^\dagger H_u \right)^2 + \frac{\lambda_2}{2} \left(H_d^\dagger H_d \right)^2 \\
& + \lambda_3 \left(H_u^\dagger H_u \right) \left(H_d^\dagger H_d \right) \\
& + \lambda_4 \left(H_u^\dagger H_d \right) \left(H_d^\dagger H_u \right) + \frac{\lambda_5}{2} \left\{ \left(H_u^\dagger H_d \right)^2 + \text{h.c.} \right\} \\
& + \frac{m_S^2}{2} S^2 + \frac{\lambda_6}{8} S^4 + \frac{\lambda_7}{2} \left(H_u^\dagger H_u \right) S^2 \\
& + \frac{\lambda_S}{2} \left(H_d^\dagger H_d \right) S^2,
\end{aligned}
\tag{14}
$$

where H_u and H_d are doublet fields similar to the NMSSM ones. This potential has a generic form and observes two symmetries: i) a Z_2-symmetry, $H_u \to H_u$, $H_d \to -H_d$, $S \to S$, which is softly broken by the term containing m_{12}^2, and ii) a spontaneously broken Z_2'-symmetry, $H_u \to H_u$, $H_d \to H_d$, $S \to -S$.

The charge assignments of the fermions under the Z_2 symmetry define the four *types* of the underlying (N)2HDM. Our adopted notation for the doublet Higgs fields is intended to indicate the Type-II N2HDM specifically, wherein the fermions have Z_2 charges such that the doublet H_u couples only to the up-type quarks and H_d to the down-type quarks and charged leptons. Upon EWSB, the two doublet fields are expanded around their respective VEVs according to Eq. (9), while the real singlet is expanded in this model as $S = v_S + S_R$. After minimisation of the potential and rotation of the scalar mass matrix, as in the NMSSM, the masses of the three physical CP-even Higgs states are obtained, with $m_{H_1} < m_{H_2} < m_{H_3}$. Besides these, the Higgs sector of the model also contains a CP-odd Higgs boson A. The Type-II N2HDM is thus essentially the non-Supersymmetic counter-part of the NMSSM, with fewer symmetries impinging on the properties of the CP-even Higgs sector, which makes it a more suitable fit for our comparative investigation than the other N2HDM types. For details of the Higgs sector of the N2HDM, we refer the reader to Refs. [33,34].

There are twelve free parameters in the potential in Eq. (14): $\lambda_{1,\cdots,7,S}$, $m_{H_u}^2$, $m_{H_d}^2$, m_S^2, m_{12}^2. Relations between these parameters and the VEVs, arising from the minimisation conditions of the Higgs potential, allow us to trade $m_{H_u}^2$, $m_{H_d}^2$, and m_S^2 for $\tan\beta$, $v\left(\equiv \sqrt{v_u^2 + v_d^2} \right)$ and v_S. Moreover, the eight quartic couplings can be traded for the physical masses, $m_{H_{1,2,3}}$, $m_{H^\pm}$, m_A, and the three independent parameters of the mixing matrix $\mathcal{R}$ in Eq. (10). These parameters, taken to be $\mathcal{R}_{11}$, $\mathcal{R}_{12}$ and $\mathcal{R}_{23}$, can then further be replaced by the top-Yukawa and gauge couplings of the H_1, defined in units of the corresponding couplings of the

Higgs boson in the SM as

$$g_{H_1tt} = \frac{\mathcal{R}_{12}}{\sin\beta}, \qquad g_{H_1VV} = \cos\beta\,\mathcal{R}_{11} + \sin\beta\,\mathcal{R}_{12}. \quad (15)$$

Thus, for the purpose of this study, the following independent real parameters representing the N2HDM were randomly scanned in the given ranges using the public tool `ScannerS-2` [35,36]:

$$m_A : 500\text{-}1000\,\text{GeV}, \quad m_{H^\pm} : 500\text{-}1000\,\text{GeV},$$
$$m_{12}^2 : 10^4\text{-}10^5\,\text{GeV}^2, \quad \tan\beta : 1\text{-}20,$$
$$g_{H_1VV}^2, g_{H_1t\bar{t}}^2 : 0.64\text{-}1.44, \quad \text{sign}(\mathcal{R}_{13}) : \pm,$$
$$\mathcal{R}_{23} : -1\text{-}1, \quad v_S : 1500\text{-}2500\,\text{GeV}, \quad (16)$$

where sign$(\mathcal{R}_{13})$ takes into account the sign ambiguity in the neutral scalar mixing. In this model, the Higgs trilinear couplings $g_{H_2H_1H_1}$ and $g_{H_3H_1H_1}$, which are of particular relevance for the process of our interest here, are given as

$$g_{H_jH_iH_i} = \frac{3}{v}\Bigg[-\frac{1}{2}\tilde{\mu}^2\left(\frac{\mathcal{R}_{i2}}{\sin\beta} - \frac{\mathcal{R}_{i1}}{\cos\beta}\right)$$
$$\times \left(6\mathcal{R}_{i2}\mathcal{R}_{j2} + 6\mathcal{R}_{i3}\mathcal{R}_{j3}\sin^2\beta\right.$$
$$\left.+ \sum_k \epsilon_{ijk}\mathcal{R}_{k3}\sin 2\beta\right)$$
$$+ \frac{2m_{H_i}^2 + m_{H_j}^2}{v_S}\left(\mathcal{R}_{i3}^2\mathcal{R}_{j3}v + \mathcal{R}_{i2}^2\mathcal{R}_{j2}\frac{v_S}{\sin\beta}\right.$$
$$\left.+ \mathcal{R}_{i1}^2\mathcal{R}_{j1}\frac{v_S}{\cos\beta}\right)\Bigg], \quad (17)$$

where $\tilde{\mu}^2 \equiv \frac{m_{12}^2}{\sin\beta\cos\beta}$ and ϵ_{ijk} is the totally antisymmetric tensor, with $\epsilon_{123} = 1$.

While the above ranges were mostly guided by existing literature on the model (see, e.g., Refs. [34,37,38]), the ones of $g_{H_1VV}^2$ and $g_{H_1t\bar{t}}^2$ were based loosely on the current 2σ error-bar on the measurements of the corresponding couplings for the h_{obs} at the LHC [39]. Several scans were performed for this model, in all of which we fixed $v = 246\,\text{GeV}$ and $m_{H_1} = 125\,\text{GeV}$. The values of $m_{H_{2,3}}$, in contrast, were set to certain different values of interest in different scans (as will be explained in the next section). The purpose of the numerical scanning was to find configurations of the parameters in Eq. (16) that satisfied theoretical conditions such as unitarity and vacuum stability, and were at the same time consistent with precision EW and B-physics measurements. In addition to these checks performed internally by `ScannerS`, testing of the Higgs sector observables against the exclusion bounds from direct collider searches was also performed for each scanned point, by interfacing it with `N2HDECAY` [40] and `HiggsBounds`. Finally, `ScannerS` was also interfaced with the program `HiggsSignals-2`

[41,42], which performs a χ^2-fit of the h_{obs} properties for a given model point against the LHC measurements, and rules it out if $\Delta\chi^2 = \chi^2_{\text{N2HDM}} - \chi^2_{\text{SM}} > 6.18$ (assuming a 2σ Gaussian error on the best-fit value).

3.3 Cross section calculation

For the output points from the scans, we proceeded to calculate the inclusive $pp \rightarrow H_1H_1$ cross section, using a `FORTRAN` code prepared in-house. For evaluating σ_{LO} given in Eq. (1), the expressions corresponding to the triangle and box form factors were formulated following the public code `HPAIR-v2.00` [20,43,44], which includes only the SM and the MSSM. The numerical computation of the next-to-LO (NLO) corrections to σ_{LO}, which can be expressed as [43]

$$\Delta\sigma = \Delta\sigma_{\text{virt}} + \Delta\sigma_{gg} + \Delta\sigma_{gq} + \Delta\sigma_{\bar{q}q}, \quad (18)$$

were also imported from `HPAIR`, since they are generic to all models. Besides catering to models beyond the MSSM, another significant way that our cross section calculator differs from `HPAIR`, which evaluates individual BW propagators for each intermediate Higgs boson in the triangle diagram, is in the incorporation of the full propagator matrix of Eq. (7). This allows us to estimate the magnitude of the effects resulting from the off-diagonal terms in the matrix, by including or neglecting these during the cross section computation for a given point by our code.

Since the input parameters as well as the particle contents, and hence the Higgs self-energy contributions, of the NMSSM and N2HDM are mutually rather different, we prepared a separate code for each of these models. In order to check the accuracy and consistency of our base code, we compared the $pp \rightarrow H_1H_1$ cross sections calculated in the MSSM limit of the NMSSM for a few test points with the ones obtained from `HPAIR`. We found the two sets of results to be in very good (within 1%) agreement. Note here that the higher order QCD corrections for this process have now been evaluated up to the next-to-next-to-next-to-LO [45–50] in the SM. We presume that these can be extended straightforwardly to the multi-Higgs models discussed here, and their overall impact would amount to a simple rescaling of our NLO calculations.

4 Analysis results

To quantify the magnitude of the triangle-box interference arising in the $S_z = 0$ channel and, additionally, the full-propagator effects within the triangle diagram, we calculated the integrated cross sections corresponding to the following cases for each successful point from the scans for the two models:
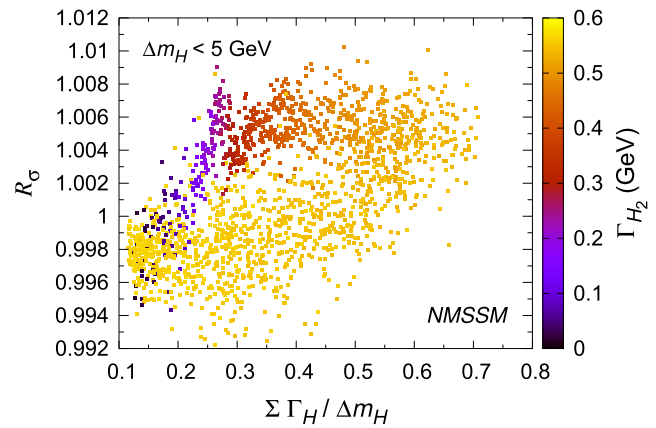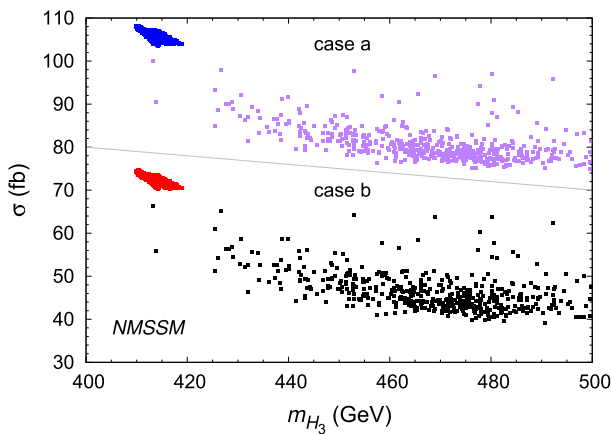
Fig. 3 Left – Cross sections corresponding to the cases a (top half) and b (bottom half) for the scanned NMSSM points, with those shown in blue and red in the respective halves being the ones with $\Delta m_H < 5$ GeV. Right – The ratio of the cross sections b and c as a function of the ratio of the sum of the widths of H_2 and H_3 and their mass difference, with the colour map showing the width of H_2, for the points with $\Delta m_H < 5$ GeV

(a) without triangle-box interference, with diagonal-only propagator matrix,

(b) with triangle-box interference, with diagonal-only propagator matrix,

(c) with triangle-box interference, with full propagator matrix.

Below, these three cross sections will be referred to as σ_a, σ_b, and σ_c, respectively. We also define $R_\sigma \equiv \sigma_b/\sigma_c$.

4.1 The NMSSM

The top half of Fig. 3 (left) shows the cross sections σ_a (top half) and σ_b (bottom half) with diagonal-only propagator matrix, as functions of the H_3 mass. One sees a large negative impact of the triangle-box interference, reducing the cross section uniformly by ~ 35 fb for all the points. We note here that, in models with Supersymmetry, the box and triangle diagrams in principle include loops from squarks also. Here we take the view that the squarks are always too heavy to contribute significantly to either of these production processes (recall that we fixed the soft squark masses to 3 TeV in our parameter space scans, to prevent the physical sparticle masses from conflicting with the direct search results from the LHC), and thus retain only the quark loops. A detailed study of the impact of the inclusion of squarks in the MSSM and the NMSSM (without the Higgs propagator interference effects) can be found in Refs. [51–53]. The small blue and red islands near the lowest allowed m_{H_3} and with overall largest cross sections in the top and bottom halves, respectively, are the points with $\Delta m_H < 5$ GeV obtained from the secondary scan.

In the numerical calculation of the propagator matrix, in contrast, the (one-loop) Higgs self-energies due to all the relevant NMSSM particles were included. The right panel of Fig. 3, however, shows negligible impact of introducing the full propagator matrix. This figure, restricted only to the points with $\Delta m_H < 5$ GeV, shows R_σ against the ratio of the sum of H_2 and H_3 widths, $\sum \Gamma_H$, and Δm_H. Note that, for a more accurate picture, the widths used for producing this plot are the higher order ones output by `NMSSMTools`, rather than the tree-level ones corresponding to the self-energies computed by our cross section code. $\sum \Gamma_H$ ranges between 535 MeV and 565 MeV for all the points, implying that when Γ_{H_2}, depicted by the colour map in the figure, reaches its maximum value, Γ_{H_3} is at its minimum, and vice versa. The fact that the lowest Δm_H obtained is 0.8 GeV, according to Eq. (13), implies that $\sum \Gamma_H / \Delta m_H$ is always smaller than 1 and hence the above mentioned condition of larger $\sum \Gamma_H$ than Δm_H for a sizeable enhancement in the propagator effects is never met. Still, one can notice a small gradual increase in R_σ, meaning an increasing negative effect of the full propagator, as $\sum \Gamma_H$ rises with respect to Δm_H. This effect is more pronounced for points with H_2 and H_3 widths closer to each other in magnitude, as illustrated by the violet/red points in the top left quadrant of the figure. A larger gap between these two widths, in contrast, generally tends to slightly increase σ_c compared to σ_b (the points in the bottom left quadrant).

The overall smallness of R_σ in the NMSSM can be attributed partly to the large squark and slepton masses, so that their contribution to the Higgs self-energies is diminished, and partly to the specific Yukawa and gauge coupling combinations of the H_2 and H_3 in the narrow parameter space region yielding large mass degeneracy between these.
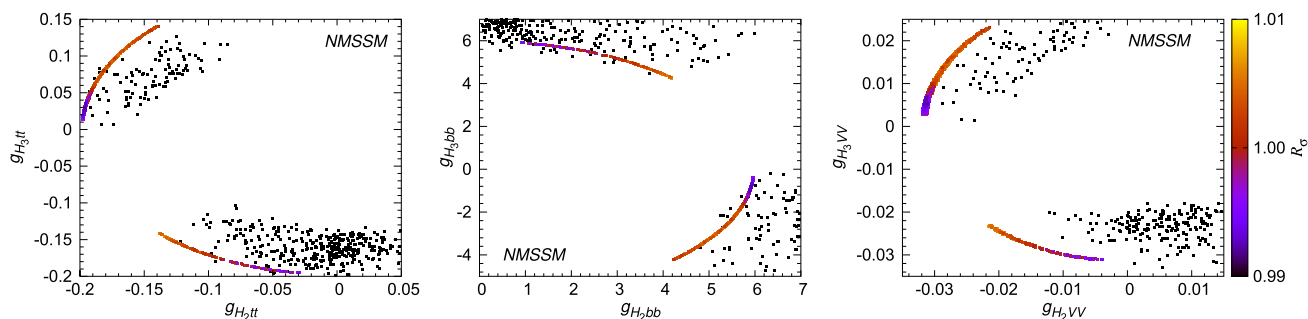
Fig. 4 H_2 and H_3 couplings to $t\bar{t}$ (left), $b\bar{b}$ (centre) and VV (right) pairs in the NMSSM, with the colour map showing the ratio of the cross sections corresponding to cases b and c for the points with $\Delta m < 5\,\text{GeV}$

Fig. 4 shows R_σ as a function of these coupling combinations. One notices in these figures that the colour-mapped points, which correspond to the parameter space region with $\Delta m_H < 5\,\text{GeV}$, mark the boundaries of the (black) points from the extended scan. Thus, the search results from the LHC, besides directly constraining the mass of the H_3 to lie above $\sim 405\,\text{GeV}$, also restrict its top-Yukawa coupling to fairly small values, with either sign. The condition of mass degeneracy with H_3 then also dictates the signs and sizes of the H_2 couplings.

According to the left panel of Fig. 4, while the H_2 and H_3 top-Yukawa couplings can take up three different sign combinations in general, for points with $\Delta m_H < 5\,\text{GeV}$, the sign of $g_{H_2 t \bar{t}}$ is always negative, while that of $g_{H_3 t \bar{t}}$ can be both negative or positive. However, only positive $g_{H_3 t \bar{t}}$ values appear for large negative values of $g_{H_2 t \bar{t}}$. As the magnitude of the latter drops, that of the former increases, with R_σ also rising slowly, until both reach equal values (with opposite signs). At that point, the sign of $g_{H_3 t \bar{t}}$ flips to negative, giving the largest R_σ according to the colour map. A further increase in its magnitude, however, along with a decrease in the size of $g_{H_2 t \bar{t}}$, leads to a lowering of R_σ again. In short, largest (allowed) values of one of the two top-Yukawa couplings, whether positive or negative, coupled with the smallest value of the other, results in $\sigma_c > \sigma_b$ and, as the two tend towards each other, σ_c starts to lower towards σ_b and eventually below it.

The central panel of the figure likewise illustrates the impact of the variations in $g_{H_2 b \bar{b}}$ and $g_{H_3 b \bar{b}}$ on R_σ. Note that the points in the bottom half of this plot correspond to the points in the top half of the left panel, and vice versa. Thus, the sign of the bottom-Yukawa coupling of a given Higgs boson is always opposite to that of its top-Yukawa coupling, so that $g_{H_2 b \bar{b}}$ is positive only, conversely to $g_{H_2 t \bar{t}}$. Furthermore, R_σ shows a similar trend with the variation in the sizes of $g_{H_2 b \bar{b}}$ and $g_{H_3 b \bar{b}}$ as with the top-Yukawa couplings – the largest (allowed) value of one bottom-Yukawa coupling paired with the smallest value of the other yields $\sigma_c > \sigma_b$, while $\sigma_c \leq \sigma_b$ results from their comparable mag-

nitudes. The dependence of R_σ on the relative signs and magnitudes of $g_{H_2 VV}$ and $g_{H_3 VV}$ follows the behaviour of the top-Yukawa couplings exactly, as seen in the right panel of the Fig. 4. Their allowed values are, however, much smaller than even those of the top-Yukawa couplings, pointing towards the decoupling regime of the (N)MSSM. As for the remaining couplings of the H_2 and H_3, even when the corresponding (s)particles have sufficiently low masses, including A_1 as well as $\chi_{1,2}^0$ and $\chi_1^\pm$ (which are higgsino-like and thus have masses $\sim \mu_{\text{eff}} \sim 150\,\text{GeV}$, see Eq. (13)), their influence on R_σ is too small to merit a discussion here.

4.2 The Type-II N2HDM

As indicated earlier, the Higgs boson masses are input parameters in the N2HDM, which allows us to investigate H_2 and H_3 with exactly equal masses, that can also be much lower than those obtained in the NMSSM. For a direct comparison with the NMSSM though, in our first scan for this model we set $m_{H_2} = m_{H_3} = 410\,\text{GeV}$, and the σ_a and σ_b for the 100 successful points thus obtained are shown in blue and red, respectively, in the left panel of Fig. 5 against the width of H_3. Contrary to the NMSSM, triangle-box interference does not reduce the cross section uniformly for all the points. While for most of the points σ_b is smaller by a few tens of fb than σ_a, the former is larger than the latter by upto 10 fb for a few points. This is owing to the wider ranges of magnitudes as well as sign combinations for the H_2 and H_3 couplings being available in this model, as will be explained later. Notice also that Γ_{H_2} can reach a few GeVs and, in fact, Γ_{H_3} can simultaneously be quite large, as illustrated by the horizontal axis of the right panel of the figure. Once again, $\Gamma_{H_{2,3}}$ here are the widths output by ScannerS, instead of the tree-level ones that can be obtained from the one-loop self-energies computed by our code. The vertical axis of this panel shows the impact of including the full propagator matrix in the cross section calculation.

For a number of points from the first scan with $m_{H_2} = m_{H_3} = 410\,\text{GeV}$, seen in red in Fig. 5 (right), σ_b is a few
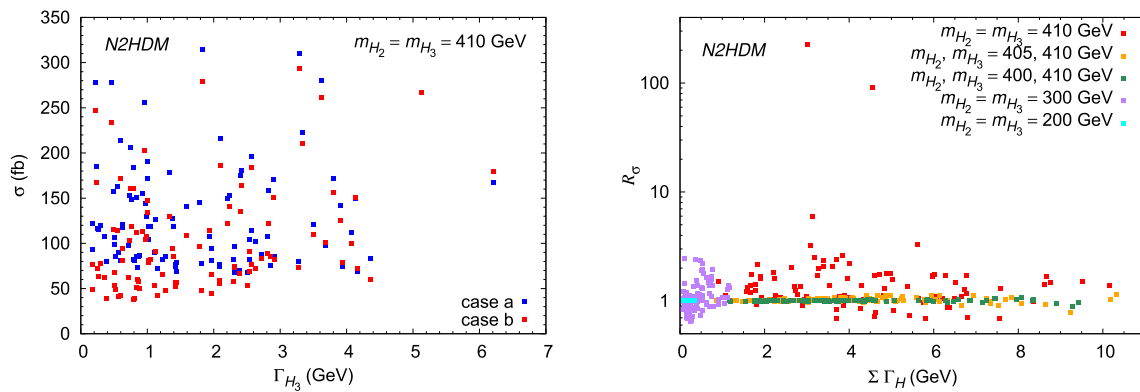
Fig. 5 Left – Cross sections for the points obtained from the N2HDM parameter space scan with $m_{H_2} = m_{H_2} = 410$ GeV, corresponding to the cases a (blue) and b (red) as functions of Γ_{H_3}. Right – The ratio of the cross sections b and c against the sum of the widths of H_2 and H_3 for the points obtained from the five N2HDM scans with different m_{H_2} and m_{H_3} configurations

times larger than σ_c, but for some points it gets reduced by upto 35%, implying a net positive contribution from the off-diagonal terms in the matrix. For two of the red points, though, R_σ exceeds 100, meaning a two orders of magnitude reduction in σ_b. (We point out here that these two points were omitted from the left panel to keep the y-axis scale visually interesting, but the corresponding cross sections will be provided below.) To assess the effect of reducing the mass degeneracy, the points from scans with $\Delta m_H = 5$ GeV and $\Delta m_H = 10$ GeV, with m_{H_3} still fixed to 410 GeV, are also plotted in this figure in orange and green, respectively. Evidently, a larger Δm_H results in smaller fluctuations in σ_b, as the R_σ value lies very close to 1 for all the 100 green points. The violet points in the figure correspond to the scan with $m_{H_2} = m_{H_3} = 300$ GeV. While in general R_σ can deviate substantially from 1 for these points also, its maximum value does not exceed 3. The main reason for this is that the widths of H_2 and H_3 are always lower than 1 GeV in this case, unlike the $m_{H_2} = m_{H_3} = 410$ GeV case, owing to the fact that their masses lie below the $t\bar{t}$ production threshold. Lowering m_{H_2} and m_{H_3} even further to under the $H_1 H_1$ threshold expectedly results in a vanishing impact of the off-diagonal propagator matrix terms, as demonstrated by the cyan points in the figure, which are all clustered together below $\sum \Gamma_H \lesssim 200$ MeV.

For a detailed investigation, we selected six Benchmark Points (BPs) from our main scan with $m_{H_2} = m_{H_3} = 410$ GeV. The input parameters, the widths and couplings of H_2 and H_3 as well as the four cross sections corresponding to these points are given in Table 2. $\sigma_{2\times 2}$ in the table implies the cross section obtained by setting $m_{H_3} \to \infty$ (in order to decouple the H_3), with all the other input parameters fixed to their exact values for a given BP, and is quoted for reference. BP1 and BP2 are the two points with the highest R_σ in Fig. 5, for BP3 and BP4 the R_σ value lies very close to 1 while BP5

and BP6 are chosen from amongst the points for which σ_c is slightly enhanced compared to σ_b.

In the 2HDM, and the N2HDM by extension, of the type-II, the B-physics measurement strongly constrain $m_{H^\pm}$ [34, 54] and therefore the latter lies above 600 GeV for all the successful points from the scans, while $\tan\beta$ is also pushed to smaller values, as can be noted in the table. m_A is then also restricted to values close to $m_{H^\pm}$ by the EW precision constraints. One feature distinguishing the points with the largest R_σ (BP1 and BP2) from the rest of the BPs are the larger $m_{H^\pm}$ and $g_{H_1 t\bar{t}}$ values and relatively small $\tan\beta$. Such parameter configurations result in specific combinations of the couplings of H_2 and H_3 for BP1 and BP2, which in turn lead to very high R_σ for these. For these two points, $g_{H_2 t\bar{t}}$ and $g_{H_3 t\bar{t}}$ are both positive and large while $g_{H_2 b\bar{b}}$, $g_{H_3 b\bar{b}}$, $g_{H_2 VV}$ and $g_{H_3 VV}$ are all negative. In the case of BP3, $g_{H_2 t\bar{t}}$ and $g_{H_3 t\bar{t}}$ have signs opposite to each other while $g_{H_2 b\bar{b}}$ and $g_{H_3 b\bar{b}}$ are both negative. We note here that, again in contrast with the NMSSM, $g_{H_2 b\bar{b}}$ is negative for all the 100 N2HDM points for the $m_{H_2} = m_{H_3} = 410$ GeV scenario, and also that, for a majority of these points, three out of the four Yukawa couplings had the same signs. BP4 and BP5 are very similar points in that the two top-Yukawa couplings have signs that are opposite not only to each other but also to the signs of the corresponding bottom-Yukawa couplings. BP6 is the only point of its kind found in the scan, with $g_{H_2 t\bar{t}}$, $g_{H_3 t\bar{t}}$ and $g_{H_2 b\bar{b}}$ all having negative signs, and it therefore uniquely exhibits a constructive triangle-box interference as well as constructive propagator interference, so that $\sigma_a < \sigma_b < \sigma_c$.

In Figs. 6 and 7 we show the four cross sections as functions of the most important H_2 couplings in this context, for all the six BPs. The former corresponds to the couplings $g_{H_2 t\bar{t}}$ and $g_{H_2 b\bar{b}}$, and the latter to $g_{H_2 VV}$ and $g_{H_2 H_1 H_1}$, while rows 1, 2, 3 and 4 in both the figures depict $\sigma_{2\times 2}$, σ_b, σ_c and R_σ, respectively. The plotted ranges of the couplings are indica-

Table 2 Values of the input parameters, couplings and widths of the Higgs bosons, together with the cross sections corresponding to the six selected BPs of the N2HDM

| Parameter/observable	BP1	BP2	BP3	BP4	BP5	BP6
m_A (GeV)	712.2	772.67	640.04	601.21	658.33	630.11
$m_{H^\pm}$ (GeV)	709.04	776.41	654.53	604.04	663.11	654.45
m_{12}^2 (GeV^2)	84725.4	71277.6	82115.1	61133.1	69580.1	65586.7
$\tan\beta$	1.3	1.0	1.3	2.0	1.8	1.2
$g_{H_1 t\bar{t}}$	1.024	1.038	0.955	0.981	0.989	0.986
$g_{H_1 VV}$	1.000	1.000	0.954	0.990	1.000	0.930
sign($\mathcal{R}_{13}$)	−	+	−	+	−	+
$\mathcal{R}_{23}$	−0.671	−0.569	−0.921	0.887	0.436	0.870
v_S (GeV)	1511.3	2357.5	1945.8	1667.5	2025.9	2459.4
$g_{H_2 t\bar{t}}$	0.545	0.766	−0.092	0.106	0.533	−0.089
$g_{H_3 t\bar{t}}$	0.505	0.509	0.805	−0.533	−0.203	−0.827
$g_{H_1 b\bar{b}}$	0.959	0.956	0.952	1.024	1.030	0.846
$g_{H_2 b\bar{b}}$	−0.984	−0.879	−0.636	−0.998	−1.490	−0.771
$g_{H_3 b\bar{b}}$	−0.880	−0.627	−1.202	1.684	0.831	1.091
$g_{H_2 VV}$	−0.029	−0.024	−0.289	−0.120	0.038	−0.362
$g_{H_3 VV}$	−0.143	−0.037	0.077	−0.079	0.038	−0.061
$g_{H_1 AA}$	82.120	111.190	56.667	51.450	66.070	61.080
$g_{H_2 AA}$	−2.585	−3.303	−22.422	−9.804	2.731	−30.780
$g_{H_3 AA}$	−1.142	−4.892	6.175	−3.003	3.429	−3.474
$g_{H_1 AZ}, g_{H_1 H^+ W^-}$	−0.031	−0.041	−1.398	0.018	0.017	−0.069
$g_{H_2 AZ}, g_{H_2 H^+ W^-}$	−0.741	−0.822	−0.262	−0.446	−0.899	−0.334
$g_{H_3 AZ}, g_{H_3 H^+ W^-}$	−0.671	−0.568	−0.965	0.895	−0.437	0.940
$g_{H_1 H^+ H^-}$	81.039	112.584	60.978	52.263	67.588	68.084
$g_{H_2 H^+ H^-}$	−2.554	−3.336	−23.728	−9.903	2.788	−33.502
$g_{H_3 H^+ H^-}$	−1.127	−4.943	6.523	−3.068	3.487	−3.930
$g_{H_1 H_1 H_1}$	3.006	3.319	4.774	7.359	7.472	0.159
$g_{H_1 H_1 H_2}$	−1.512	−1.260	−6.579	−2.557	1.404	−7.562
$g_{H_1 H_1 H_3}$	−1.083	−1.351	1.709	−2.238	0.666	−0.206
$g_{H_1 H_2 H_2}$	0.314	5.460	2.100	2.411	1.883	7.209
$g_{H_1 H_2 H_3}$	0.325	3.736	−0.231	−1.453	−0.954	−1.479
$g_{H_1 H_3 H_3}$	0.226	2.682	1.249	4.826	0.296	8.859
$g_{H_2 H_2 H_2}$	−63.753	−46.913	−30.048	−44.402	−95.745	−22.313
$g_{H_2 H_2 H_3}$	3.092	0.163	−0.700	6.525	1.830	7.870
$g_{H_2 H_3 H_3}$	−3.725	−3.740	−4.920	−2.443	1.860	−8.990
$g_{H_3 H_3 H_3}$	−50.644	−27.989	−74.038	98.871	53.169	55.571
Γ_{H_2} (GeV)	1.63	3.13	3.15	0.58	1.58	4.67
Γ_{H_3} (GeV)	1.38	1.43	3.62	1.78	0.27	3.68
$\sigma_{2\times 2}$ (fb)	122.9	99.2	102.9	204.9	93.0	120.7
σ_a (fb)	35518.6	13465.4	280.4	144.9	115.8	98.0
σ_b (fb)	34536.1	13417.6	260.1	96.6	62.9	101.3
σ_c (fb)	154.3	146.7	153.1	96.2	63.6	102.6
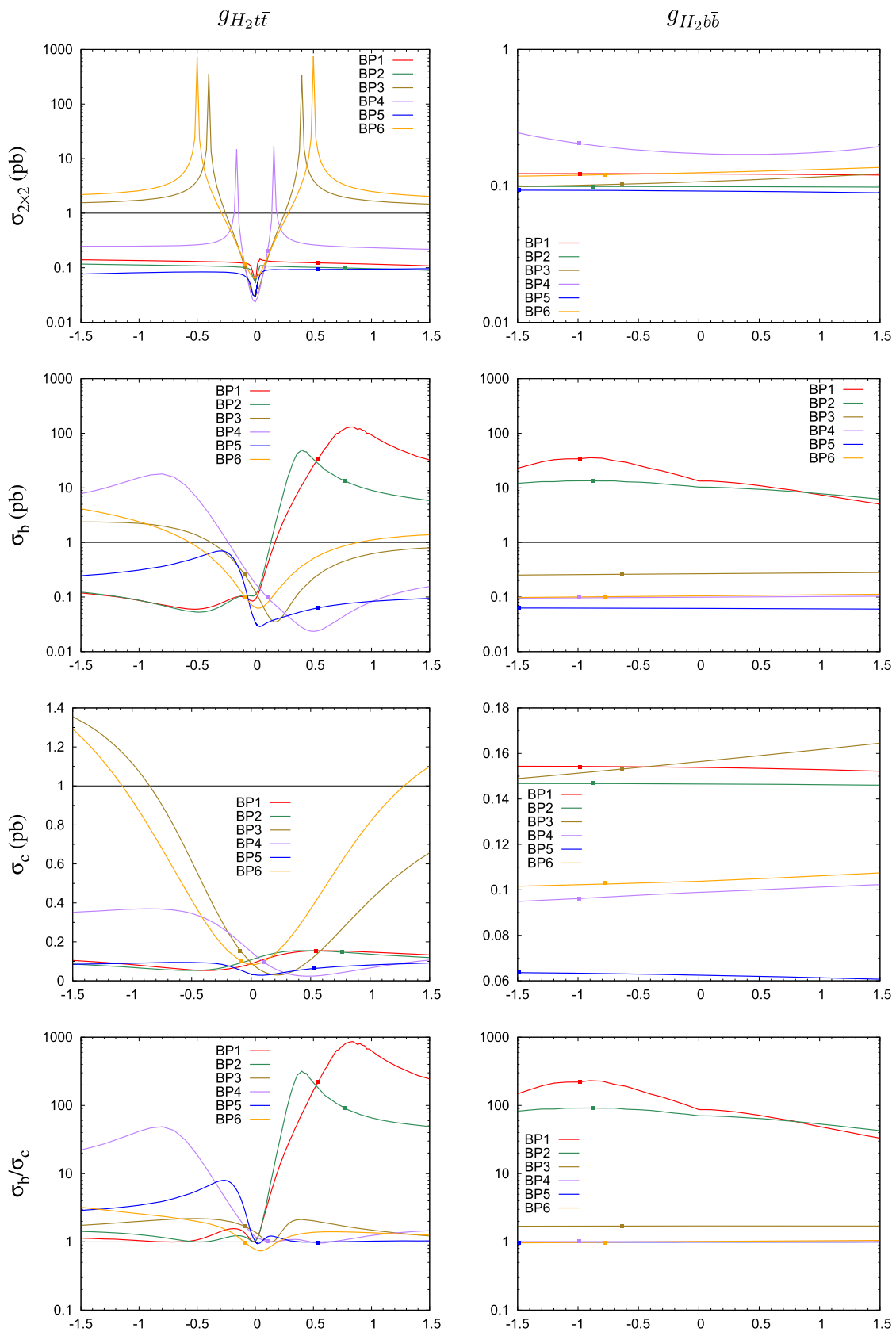
Fig. 6 Various cross sections as functions of the couplings $g_{H_2 t\bar{t}}$ (left) and $g_{H_2 b\bar{b}}$ (right). The point on a line marks the actual value of the plotted coupling for the corresponding BP. See text for more details
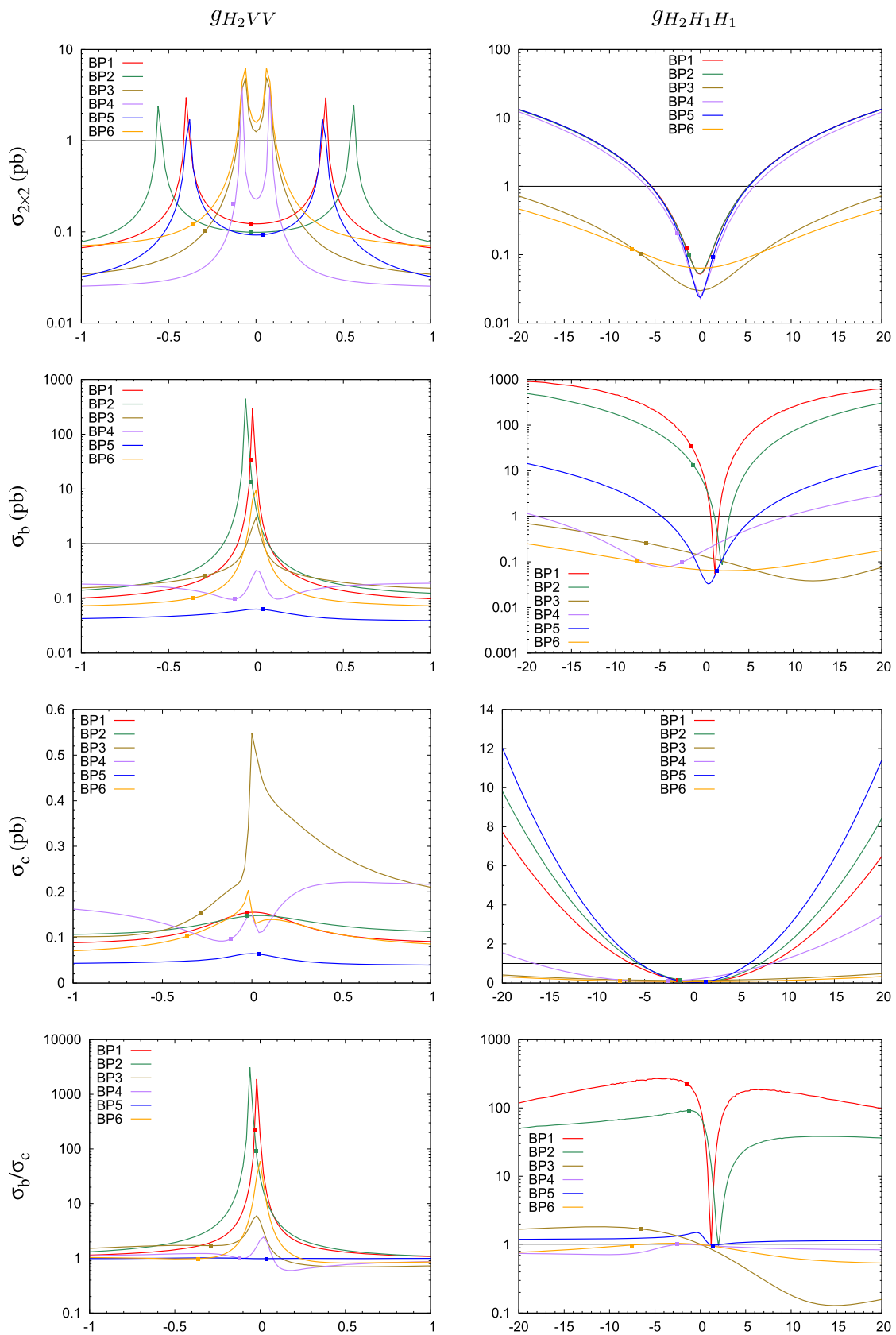
Fig. 7 Various cross sections as functions of the couplings g_{H_2VV} (left) and $g_{H_2H_1H_1}$ (right). The point on a line marks the actual value of the plotted coupling for the corresponding BP. See text for more details

tive of those observed across all the 100 points obtained for the $m_{H_2} = m_{H_3} = 410\,\text{GeV}$ scenario. Once again, for each BP in a given panel, all the remaining couplings are fixed to the values described in Table 2. The red lines in the figure correspond to BP1, green to BP2, olive to BP3, violet to BP4, blue to BP5 and orange to BP6. The point on a line in a given panel marks the actual value of the plotted coupling for that BP. The horizontal black lines in the panels in columns 1, 2 and 3, indicate the current experimental limit on h_{obs} pair-production cross section [55], which we approximate to be $1\,\text{pb}$ for $m_{H_2} = m_{H_3} = 410\,\text{GeV}$ considered here. Note also that, since only the product of the corresponding H_2 and H_3 couplings enters the $i\Im\hat{\Pi}_{23}(\hat{s})$ element of the Higgs propagator matrix, the behaviour of σ_c with varying H_3 couplings should by and large mimic that with varying H_2 couplings.

In the left column of the Fig. 6, one sees that the presence of an additional Higgs boson degenerate in mass with H_2 eliminates the peaks appearing at specific values of $g_{H_2 t\bar{t}}$ in $\sigma_{2\times 2}$, so that the variations in σ_b in the second row are smoother than in the first row. As expected, σ_b shows a very similar behaviour for BP1 and BP2, reaching values even higher than the true ones for slightly different positive $g_{H_2 t\bar{t}}$ (recall that $g_{H_3 t\bar{t}}$ is also positive for these two points). Thus $g_{H_2 t\bar{t}} \gtrsim 0.1$ would be ruled out by the LHC $h_{\text{obs}}h_{\text{obs}}$-production limits. When $g_{H_2 t\bar{t}}$ switches sign to negative, σ_b drops to much smaller values. The introduction of the full propagator matrix then largely mitigates the very strong dependence of the cross section on positive $g_{H_3 t\bar{t}}$, as seen in the third row, bringing it down to values with experimental bounds. And since σ_c shows little variation with $g_{H_2 t\bar{t}}$, the shapes of the red and green lines in the bottom row of this column (and also of the right column) are very similar to those in row 2, with R_σ reaching about 900 for the BP1.

Cross sections for BP3 and BP4, both of which have $g_{H_3 t\bar{t}}$ with mutually opposite signs but very similar magnitudes, show similar trends to each other with the variations in $g_{H_2 t\bar{t}}$ across the four panels on the left. For these two points, the peaks in $\sigma_{2\times 2}$ are the tallest, while σ_b and even σ_c violates the experimental bound for large negative $g_{H_2 t\bar{t}}$. BP4 and BP5, likewise mimic each other's behaviour for positive $g_{H_2 t\bar{t}}$, but since BP4 has a negative $g_{H_3 t\bar{t}}$ larger in magnitude than that in BP5, its dependence on negative $g_{H_2 t\bar{t}}$ is much more pronounced for both σ_b and σ_c. The right column of the figure shows negligible dependence of σ_b on $g_{H_2 b\bar{b}}$ for all the BPs expect 1 and 2 and, conversely, the least variation in σ_c for these two BPs. This is due to the fact that for these points $g_{H_2 b\bar{b}}$ and $g_{H_3 b\bar{b}}$ both have negative signs, opposite to the signs of the two top-Yukawa couplings which have a much more dominant effect.

The left column of Fig. 7 illustrates that the $g_{H_2 VV}$ coupling plays a role as crucial as the top-Yukawa couplings. Similarly to the NMSSM, these couplings originally have generally quite small magnitudes, as a consequence of the

very SM-like properties of the H_1. For this coupling, the two peaks appearing in $\sigma_{2\times 2}$ are replaced by a tall narrow peak in σ_b, close to $g_{H_2 VV} = 0$. The introduction of the full propagator matrix brings even the highest of all the peak values of σ_b, seen for BP1 and BP2, down to an experimentally acceptable sub-pb level. The shapes of all the lines are hence largely dictated by the interplay between the signs and sizes of the top-Yukawa and gauge couplings of H_2 and H_3. In the right column is depicted the dependence of the cross sections on $g_{H_2 H_1 H_1}$, which is the only coupling of significance other than the ones discussed above. Here, $\sigma_{2\times 2}$ shows a sharp dip at the zero of this coupling, since it also enters the $H_2 \rightarrow H_1 H_1$ decay besides the self-energies. This sharp dip shifts away from zero for σ_b, according to the relative sign of the diagonal H_3 contributions to the propagator. It returns to zero when the off-diagonal terms are also turned on. Around the minimum, σ_c shows a fairly symmmetric behaviour in both signs of $g_{H_2 H_1 H_1}$, as do σ_b and σ_b. Unlike these two cross sections, however, σ_c increases rather smoothly.

Finally, a negligible dependence of each of the cross sections on all of the remaining couplings given in Table 2 was noted, since the corresponding particle pairs are rather heavy. The contribution to the Higgs self-energies from even the relatively lighter pairs, such as AZ and $H^+ W^-$, for any value of the coupling is vanishing. Plots illustrating variations in the rest of the couplings can therefore be safely dropped.

5 Conclusions

The commonly adopted approach of calculating the cross section for a given $2 \rightarrow 2$ process by factorising it into its production and decay parts cannot account for possible quantum interference amongst the propagators of several mass-degenerate states. This is because such an approach by construction assumes narrow widths for the resonant mediators. In some previous papers we explored such interference effects in the case of the gluon-fusion production of certain SM final states, via two highly mass-degenerate Higgs mediators. The mass-splitting between the two intermediate Higgs states being comparable to or smaller than the sum of their widths is a precondition for such effects to be sizeable, in both the integral and the differential cross section. The reason for their onset is that the imaginary off-diagonal elements of the Higgs propagator matrix become comparable to the imaginary parts of the diagonal elements, irrespectively of whether they are taken into account coherently or incoherently. These studies were performed within the illustrative theoretical framework of the NMSSM.

In this article, we have extended our investigation to the pair-production of the lightest of the three NMSSM neutral Higgs scalars, H_1, at the 14 TeV LHC, taking into account the contributions of the triangle as well as the box diagram

that this process proceeds through. We have investigated the impact of not only the interference between these two topologies, but also of the aforementioned propagator interference between H_2 and H_3 within the triangle topology on the cross section for $H_1 H_1$ production. Furthermore, since the lowest H_3 mass attainable in the NMSSM is 405 GeV, owing to the bounds from the LHC searches, we have also included the N2HDM in our analysis. In this framework, since the physical Higgs boson masses are input parameters, we could choose any desired (unique) value for m_{H_2} and m_{H_3}, which allowed us to study also the scenario where they contribute non-resonantly to the triangle topology for the studied process.

In the case of the NMSSM, we have found the effects of the inclusion of the full Higgs propagator matrix in the triangle topology to be similar in size to those established in our previous studies. However, given the various constraints imposed, since the minimal mass-splitting between H_2 and H_3 is obtained in a very narrow region of the parameter space where, however, the sum of their widths never exceeds it, the effect is largely subdued. In this region the box diagram and the triangle diagram with (an off-shell) H_1 in the propagator contribute much more dominantly to the H_1 pair-production process. The narrowness of this region also means that a nearly constant negative interference is always observed between the two topologies.

In the N2HDM, on the other hand, we have seen that the propagator interference effects can modify the cross section by more than two orders of magnitude. Of particular importance is the observation that these effects tend to 'regulate' the behavior of the total $H_1 H_1$ cross section, smoothing the peaks that appear in it for certain specific values of the H_2 and H_3 couplings, and generally bringing it down to values consistent with the current LHC limits. Moreover, herein the interference between the box and triangle topologies can be positive or negative, as a consequence of the relatively wider ranges of the magnitudes and sign combinations of the Higgs boson Yukawa couplings. Clearly, such a disparity between the results obtained for this model and those for the NMSSM is due to the fact that supersymmetry imposes strong limitations on the masses and couplings of the heavy Higgs states. In the N2HDM, these quantities are essentially free parameters. But even in this model, when m_{H_2} and m_{H_3} lie below the $H_1 H_1$ production threshold, the propagator interference effects tend to vanish. In this case the one-loop two-point functions corresponding to the off-diagonal elements in the Higgs propagator matrix are too small to be able to overcome the kinematic suppression.

Finally, we emphasise that we have reached the above conclusions on the basis of a detailed analysis at the level of the total cross section. As for their phenomenological relevance, the LHC may develop sensitivity to all such interesting dynamics already at its upcoming Run 3, at least in the N2HDM. Hence, for the purpose of aiding experimental efforts in establishing all the effects studied here, we have proposed some BPs, compliant with the latest theoretical and experimental constraints, that are amenable to dedicated probes by the ATLAS and CMS collaborations.

Data Availability Statement This manuscript has no associated data or the data will not be deposited. [Authors' comment: All the relevant data has been presented in the figures and tables.]

References

1. ATLAS Collaboration, G. Aad et al., Observation of a new particle in the search for the Standard Model Higgs boson with the ATLAS detector at the LHC. Phys. Lett. B **716**, 1 (2012). https://doi.org/10.1016/j.physletb.2012.08.020. arXiv:1207.7214
2. C.M.S. Collaboration, S. Chatrchyan et al., Observation of a new boson at a mass of 125 GeV with the CMS experiment at the LHC. Phys. Lett. B **716**, 30 (2012). https://doi.org/10.1016/j.physletb.2012.08.021 arXiv:1207.7235
3. G.C. Branco, P.M. Ferreira, L. Lavoura, M.N. Rebelo, M. Sher, J.P. Silva, Theory and phenomenology of two-Higgs-doublet models. Phys. Rept. **516**, 1 (2012). https://doi.org/10.1016/j.physrep.2012.02.002 arXiv:1106.0034
4. J.F. Gunion, H.E. Haber, G.L. Kane, S. Dawson, The Higgs Hunter's guide. Front. Phys. **80**, 1 (2000)
5. J.F. Gunion, H.E. Haber, G.L. Kane, S. Dawson, Errata for the Higgs hunter's guide (1992). arXiv:hep-ph/9302272
6. A. Djouadi, The Anatomy of electro-weak symmetry breaking. II. The Higgs bosons in the minimal supersymmetric model. Phys. Rept. **459**, 1 (2008). https://doi.org/10.1016/j.physrep.2007.10.005. arXiv:hep-ph/0503173
7. J.F. Gunion, H.E. Haber, The CP conserving two Higgs doublet model: the approach to the decoupling limit. Phys. Rev. D (2003). https://doi.org/10.1103/PhysRevD.67.075019. arXiv:hep-ph/0207010
8. M. Carena, I. Low, N.R. Shah, C.E.M. Wagner, Impersonating the Standard Model Higgs Boson: alignment without decoupling. JHEP **04**, 015 (2014). https://doi.org/10.1007/JHEP04(2014)015 arXiv:1310.2248

9. H.E. Haber, S. Heinemeyer, T. Stefaniak, The impact of two-loop effects on the scenario of MSSM Higgs alignment without decoupling. Eur. Phys. J. C **77**, 742 (2017). https://doi.org/10.1140/epjc/s10052-017-5243-5 arXiv:1708.04416

10. J.R. Ellis, J.S. Lee, A. Pilaftsis, CERN LHC signatures of resonant CP violation in a minimal supersymmetric Higgs sector. Phys. Rev. D (2004). https://doi.org/10.1103/PhysRevD.70.075010. arXiv:hep-ph/0404167

11. E. Fuchs, S. Thewes, G. Weiglein, Interference effects in BSM processes with a generalised narrow-width approximation. Eur. Phys. J. C **75**, 254 (2015). https://doi.org/10.1140/epjc/s10052-015-3472-z arXiv:1411.4652

12. E. Fuchs, G. Weiglein, Breit-Wigner approximation for propagators of mixed unstable states. JHEP **09**, 079 (2017). https://doi.org/10.1007/JHEP09(2017)079 arXiv:1610.06193

13. E. Fuchs, G. Weiglein, Impact of CP-violating interference effects on MSSM Higgs searches. Eur. Phys. J. C **78**, 87 (2018). https://doi.org/10.1140/epjc/s10052-018-5543-4 arXiv:1705.05757

14. P. Fayet, Supergauge invariant extension of the Higgs mechanism and a model for the electron and its neutrino. Nucl. Phys. B **90**, 104 (1975). https://doi.org/10.1016/0550-3213(75)90636-7

15. J.R. Ellis, J. Gunion, H.E. Haber, L. Roszkowski, F. Zwirner, Higgs Bosons in a nonminimal supersymmetric model. Phys. Rev. D **39**, 844 (1989). https://doi.org/10.1103/PhysRevD.39.844

16. L. Durand, J.L. Lopez, Upper bounds on Higgs and top quark masses in the flipped SU(5) x U(1) superstring model. Phys. Lett. B **217**, 463 (1989). https://doi.org/10.1016/0370-2693(89)90079-8

17. M. Drees, Supersymmetric models with extended Higgs sector. Int. J. Mod. Phys. A **4**, 3635 (1989). https://doi.org/10.1142/S0217751X89001448

18. B. Das, S. Moretti, S. Munir, P. Poulose, Two Higgs bosons near 125 GeV in the NMSSM: beyond the narrow width approximation. Eur. Phys. J. C **77**, 544 (2017). https://doi.org/10.1140/epjc/s10052-017-5096-y arXiv:1704.02941

19. B. Das, S. Moretti, S. Munir, P. Poulose, Quantum interference among heavy NMSSM Higgs bosons. Phys. Rev. D (2018). https://doi.org/10.1103/PhysRevD.98.055020. arXiv:1804.10393

20. T. Plehn, M. Spira, P. Zerwas, Pair production of neutral Higgs particles in gluon–gluon collisions. Nucl. Phys. B **479**, 46 (1996). https://doi.org/10.1016/0550-3213(96)00418-X arXiv:hep-ph/9603205

21. J. Lee, A. Pilaftsis, M.S. Carena, S. Choi, M. Drees et al., CPsuperH: A computational tool for Higgs phenomenology in the minimal supersymmetric standard model with explicit CP violation. Comput. Phys. Commun. **156**, 283 (2004). https://doi.org/10.1016/S0010-4655(03)00463-6 arXiv:hep-ph/0307377

22. J. Baglio, R. Grober, M. Muhlleitner, D. Nhung, H. Rzehak et al., NMSSMCALC: a program package for the calculation of loop-corrected Higgs Boson masses and decay widths in the (Complex) NMSSM. Comput. Phys. Commun. **185**(12), 3372 (2014). https://doi.org/10.1016/j.cpc.2014.08.005. arXiv:1312.4788

23. M.S. Carena, J.R. Ellis, A. Pilaftsis, C. Wagner, Renormalization group improved effective potential for the MSSM Higgs sector with explicit CP violation. Nucl. Phys. B **586**, 92 (2000). https://doi.org/10.1016/S0550-3213(00)00358-8 arXiv:hep-ph/0003180

24. G. Cacciapaglia, A. Deandrea, S. De Curtis, Nearby resonances beyond the Breit–Wigner approximation. Phys. Lett. B **682**, 43 (2009). https://doi.org/10.1016/j.physletb.2009.10.090 arXiv:0906.3417

25. See http://www.th.u-psud.fr/NMHDECAY/nmssmtools.html

26. U. Ellwanger, J.F. Gunion, C. Hugonie, NMHDECAY: a Fortran code for the Higgs masses, couplings and decay widths in the NMSSM. JHEP **0502**, 066 (2005). https://doi.org/10.1088/1126-6708/2005/02/066 arXiv:hep-ph/0406215

27. U. Ellwanger, C. Hugonie, NMHDECAY 2.0: An Updated program for sparticle masses, Higgs masses, couplings and decay widths in the NMSSM. Comput. Phys. Commun. **175**, 290 (2006). https://doi.org/10.1016/j.cpc.2006.04.004. arXiv:hep-ph/0508022

28. P. Bechtle, O. Brein, S. Heinemeyer, G. Weiglein, K.E. Williams, HiggsBounds: confronting arbitrary Higgs sectors with exclusion bounds from LEP and the tevatron. Comput. Phys. Commun. **181**, 138 (2010). https://doi.org/10.1016/j.cpc.2009.09.003 arXiv:0811.4169

29. P. Bechtle, O. Brein, S. Heinemeyer, G. Weiglein, K.E. Williams, HiggsBounds 2.0.0: confronting neutral and charged Higgs sector predictions with exclusion bounds from LEP and the Tevatron. Comput. Phys. Commun. **182**, 2605 (2011). https://doi.org/10.1016/j.cpc.2011.07.015. arXiv:1102.1898

30. P. Bechtle, O. Brein, S. Heinemeyer, O. Stål, T. Stefaniak et al., HiggsBounds − 4: improved tests of extended Higgs sectors against exclusion bounds from LEP, the Tevatron and the LHC. Eur. Phys. J. C **74**, 2693 (2014). https://doi.org/10.1140/epjc/s10052-013-2693-2. arXiv:1311.0055

31. P. Bechtle, S. Heinemeyer, O. Stal, T. Stefaniak, G. Weiglein, Applying exclusion likelihoods from LHC searches to extended Higgs sectors. Eur. Phys. J. C **75**, 421 (2015). https://doi.org/10.1140/epjc/s10052-015-3650-z arXiv:1507.06706

32. P. Bechtle, D. Dercks, S. Heinemeyer, T. Klingl, T. Stefaniak, G. Weiglein et al., HiggsBounds-5: Testing Higgs sectors in the LHC 13 TeV Era (2020). arXiv:2006.06007

33. S. von Buddenbrock, N. Chakrabarty, A.S. Cornell, D. Kar, M. Kumar, T. Mandal et al., Phenomenological signatures of additional scalar bosons at the LHC. Eur. Phys. J. C **76**, 580 (2016). https://doi.org/10.1140/epjc/s10052-016-4435-8 arXiv:1606.01674

34. M. Mühlleitner, M.O.P. Sampaio, R. Santos, J. Wittbrodt, The N2HDM under theoretical and experimental scrutiny. JHEP **03**, 094 (2017). https://doi.org/10.1007/JHEP03(2017)094 arXiv:1612.01309

35. R. Coimbra, M.O. Sampaio, R. Santos, ScannerS: constraining the phase diagram of a complex scalar singlet at the LHC. Eur. Phys. J. C **73**, 2428 (2013). https://doi.org/10.1140/epjc/s10052-013-2428-4 arXiv:1301.2599

36. M. Mühlleitner, M.O. Sampaio, R. Santos, J. Wittbrodt, ScannerS: parameter scans in extended scalar sectors (2020). arXiv:2007.02985

37. M. Krause, D. Lopez-Val, M. Mühlleitner, R. Santos, Gauge-independent Renormalization of the N2HDM. JHEP **12**, 077 (2017). https://doi.org/10.1007/JHEP12(2017)077 arXiv:1708.01578

38. P. Ferreira, M. Mühlleitner, R. Santos, G. Weiglein, J. Wittbrodt, Vacuum instabilities in the N2HDM. JHEP **09**, 006 (2019). https://doi.org/10.1007/JHEP09(2019)006 arXiv:1905.10234

39. C.M.S. Collaboration, A.M. Sirunyan et al., Combined measurements of Higgs boson couplings in proton–proton collisions at $\sqrt{s} = 13$ TeV. Eur. Phys. J. C **79**, 421 (2019). https://doi.org/10.1140/epjc/s10052-019-6909-y arXiv:1809.10733

40. I. Engeln, M. Mühlleitner, J. Wittbrodt, N2HDECAY: Higgs boson decays in the different phases of the N2HDM. Comput. Phys. Commun. **234**, 256 (2019). https://doi.org/10.1016/j.cpc.2018.07.020 arXiv:1805.00966

41. P. Bechtle, S. Heinemeyer, O. Stål, T. Stefaniak, G. Weiglein, *HiggsSignals*: confronting arbitrary Higgs sectors with measurements at the Tevatron and the LHC. Eur. Phys. J. C **74**, 2711 (2014). https://doi.org/10.1140/epjc/s10052-013-2711-4 arXiv:1305.1933

42. P. Bechtle, S. Heinemeyer, T. Klingl, T. Stefaniak, G. Weiglein, J. Wittbrodt, HiggsSignals-2: probing new physics with precision Higgs measurements in the LHC 13 TeV era (2020). arXiv:2012.09197

43. S. Dawson, S. Dittmaier, M. Spira, Neutral Higgs boson pair production at hadron colliders: QCD corrections. Phys.

Rev. D (1998). https://doi.org/10.1103/PhysRevD.58.115012. arXiv:hep-ph/9805244

44. R. Gröber, M. Mühlleitner, M. Spira, J. Streicher, NLO QCD corrections to Higgs pair production including dimension-6 operators. JHEP **09**, 092 (2015). https://doi.org/10.1007/JHEP09(2015)092 arXiv:1504.06577

45. A. Agostini, G. Degrassi, R. Gröber, P. Slavich, NLO-QCD corrections to Higgs pair production in the MSSM. JHEP **04**, 106 (2016). https://doi.org/10.1007/JHEP04(2016)106 arXiv:1601.03671

46. G. Degrassi, P.P. Giardino, R. Gröber, On the two-loop virtual QCD corrections to Higgs boson pair production in the standard model. Eur. Phys. J. C **76**, 411 (2016). https://doi.org/10.1140/epjc/s10052-016-4256-9 arXiv:1603.00385

47. R. Bonciani, G. Degrassi, P.P. Giardino, R. Gröber, Analytical method for next-to-leading-order QCD corrections to double-Higgs production. Phys. Rev. Lett. (2018). https://doi.org/10.1103/PhysRevLett.121.162003. arXiv:1806.11564

48. L.-B. Chen, H.T. Li, H.-S. Shao, J. Wang, Higgs boson pair production via gluon fusion at N^{3}LO in QCD. Phys. Lett. B (2020). https://doi.org/10.1016/j.physletb.2020.135292. arXiv:1909.06808

49. L.-B. Chen, H.T. Li, H.-S. Shao, J. Wang, The gluon-fusion production of Higgs boson pair: N^{3}LO QCD corrections and top-quark mass effects. JHEP **03**, 072 (2020). https://doi.org/10.1007/JHEP03(2020)072 arXiv:1912.13001

50. J. Baglio, F. Campanario, S. Glaus, M. Mühlleitner, J. Ronca, M. Spira et al., Higgs-pair production via gluon fusion at hadron colliders: NLO QCD corrections. JHEP **04**, 181 (2020). https://doi.org/10.1007/JHEP04(2020)181 arXiv:2003.03227

51. B. Batell, M. McCullough, D. Stolarski, C.B. Verhaaren, Putting a stop to di-Higgs modifications. JHEP **09**, 216 (2015). https://doi.org/10.1007/JHEP09(2015)216 arXiv:1508.01208

52. P. Huang, A. Joglekar, M. Li, C.E.M. Wagner, Corrections to di-Higgs boson production with light stops and modified Higgs couplings. Phys. Rev. D (2018). https://doi.org/10.1103/PhysRevD.97.075001. arXiv:1711.05743

53. P. Huang, Y.H. Ng, Di-Higgs production in SUSY models at the LHC. Eur. Phys. J. Plus **135**, 660 (2020). https://doi.org/10.1140/epjp/s13360-020-00677-1 arXiv:1910.13968

54. A. Arbey, F. Mahmoudi, O. Stal, T. Stefaniak, Status of the charged Higgs Boson in two Higgs doublet models. Eur. Phys. J. C **78**, 182 (2018). https://doi.org/10.1140/epjc/s10052-018-5651-1 arXiv:1706.07414

55. CMS collaboration, A.M. Sirunyan et al., Combination of searches for Higgs boson pair production in proton–proton collisions at $\sqrt{s} = 13$ TeV. Phys. Rev. Lett. **122**, 121803 (2019). https://doi.org/10.1103/PhysRevLett.122.121803. arXiv:1811.09689